EUROPEAN ORGANIZATION FOR NUCLEAR RESEARCH (CERN)

CERN-EP-2019-280
2020/01/13

CMS-EXO-18-013

Search for an excited lepton that decays via a contact interaction to a lepton and two jets in proton-proton collisions at $\sqrt{s} = 13\,\text{TeV}$

The CMS Collaboration*

Abstract

Results are presented from a search for events containing an excited lepton (electron or muon) produced in association with an ordinary lepton of the same flavor and decaying to a lepton and two hadronic jets. Both the production and the decay of the excited leptons are assumed to occur via a contact interaction with a characteristic energy scale Λ. The branching fraction for the decay mode under study increases with the mass of the excited lepton and is the most sensitive channel for very heavy excited leptons. The analysis uses a sample of proton-proton collisions collected by the CMS experiment at the LHC at $\sqrt{s} = 13\,\text{TeV}$, corresponding to an integrated luminosity of $77.4\,\text{fb}^{-1}$. The four-body invariant mass of the two lepton plus two jet system is used as the primary discriminating variable. No significant excess of events beyond the expectation for standard model processes is observed. Assuming that Λ is equal to the mass of the excited leptons, excited electrons and muons with masses below 5.6 and 5.7 TeV, respectively, are excluded at 95% confidence level. These are the best limits to date.

Submitted to the Journal of High Energy Physics

*See Appendix **??** for the list of collaboration members

1 Introduction

The standard model (SM) of particle physics accurately describes a broad range of observations, but it does not provide an explanation for many of its own features. Among the most prominent of these features is the existence of three fermion generations, encompassing both leptons and quarks. Attempts to explain the observed generation structure have led to a class of models postulating that quarks and leptons are composite objects that consist of more fundamental constituents [1–9]. In these models, the fundamental constituents are bound by an asymptotically free gauge interaction that becomes strong below a characteristic scale Λ. Such compositeness models predict the existence of excited states of quarks (q^*) and leptons (ℓ^*) at the characteristic scale of the new binding interaction. Since these excited fermions couple to ordinary SM fermions, they could be produced via contact interactions (CI) in collider experiments, with subsequent decays to SM fermions through the gauge interactions (GIs), via the emission of a W or Z boson or a photon (γ), or via a CI to other fermions.

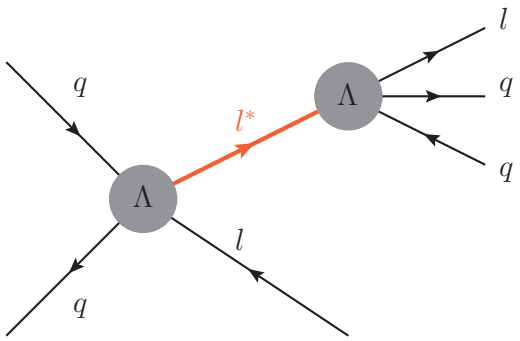

Figure 1: Feynman diagram for the production of an excited lepton in association with an SM lepton in a hadron collider. The excited lepton decays via a contact interaction to one SM lepton and two resolved jets, which result from the hadronization of the quarks.

Searches at the CERN LEP [10–13], DESY HERA [14], and the Fermilab Tevatron [15–18] have found no evidence for excited leptons. At the CERN Large Hadron Collider (LHC), previous searches performed by the ATLAS [19–21] and CMS collaborations [22, 23] have also found no evidence of excited leptons. The maximum Λ value excluded experimentally corresponds to 25 TeV (for $M_{\ell^*} \approx 1$ TeV) from a recent CMS $\ell\ell\gamma$ analysis using proton-proton (pp) collision data at $\sqrt{s} = 13$ TeV, corresponding to an integrated luminosity of 35.9 fb^{-1} [24]. The same analysis excluded excited electrons and muons with masses below 3.7 and 3.8 TeV, respectively, for $M_{\ell^*} = \Lambda$.

In this paper, a search for excited leptons (e^* and μ^*) is presented. This analysis focuses on the production of two same-flavor leptons of which one is excited and the other one corresponds to an SM lepton. The excited lepton is assumed to decay subsequently via a CI to an SM lepton of the same flavor and a quark pair, yielding two jets. The process is illustrated in Fig. 1.

The data used for this analysis were recorded with the CMS detector in pp collisions at $\sqrt{s} = 13$ TeV during 2016 and 2017 and correspond to integrated luminosities of 35.9 and 41.5 fb^{-1}, respectively, for a total of 77.4 fb^{-1}.

2 The CMS detector

The central feature of the CMS apparatus is a superconducting solenoid of 6 m internal diameter, providing a magnetic field of 3.8 T. Within the solenoid volume are a silicon pixel and strip

tracker, a lead tungstate crystal electromagnetic calorimeter (ECAL), and a brass and scintillator hadron calorimeter (HCAL), each composed of a barrel and two endcap sections. Extensive forward calorimetry complements the coverage provided by the barrel and endcap detectors.

The silicon tracker measures charged particles within the pseudorapidity range $|\eta| < 2.5$. It consists of silicon pixel and silicon strip detector modules. The electromagnetic calorimeter consists of 75 848 lead tungstate crystals that provide coverage in pseudorapidity $|\eta| < 1.48$ in a barrel region and $1.48 < |\eta| < 3.00$ in two endcap regions. The ECAL energy resolution for electrons with a transverse momentum $p_T \approx 45\,\text{GeV}$ from $Z \to ee$ decays is better than 2% in the central region of the ECAL barrel ($|\eta| < 0.8$), and is between 2 and 5% elsewhere [25]. For high energies, which are relevant for this analysis, the electron energy resolution slightly improves [26].

Muons are measured in gas-ionization detectors embedded in the steel flux-return yoke outside the solenoid, in the pseudorapidity range $|\eta| < 2.4$. Detection is provided using three technologies: drift tubes (DTs), cathode strip chambers (CSCs), and resistive-plate chambers (RPCs). While the barrel region of $|\eta| \leq 1.1$ is instrumented with DTs and RPCs, the endcaps ($1.1 < |\eta| < 2.4$) are equipped with CSCs and RPCs. A muon from the interaction point will cross four layers of muon chambers, interleaved with steel forming the return yoke of the magnetic field. Every chamber provides reconstructed hits on several detection planes, which are then combined into local track segments, forming the basis of muon reconstruction inside the muon system. Matching muons to tracks measured in the silicon tracker results in a relative transverse momentum resolution, for muons with p_T up to 100 GeV, of 1% in the barrel and 3% in the endcaps. The p_T resolution in the barrel is better than 7% for muons with p_T up to 1 TeV [27].

A particle-flow algorithm [28] aims to reconstruct and identify each individual particle in an event, with an optimized combination of information from the various elements of the CMS detector. The energy of photons is obtained from the ECAL measurement. The energy of electrons is determined from a combination of the electron momentum at the primary interaction vertex as determined by the tracker, the energy of the corresponding ECAL cluster, and the energy sum of all bremsstrahlung photons spatially compatible with originating from the electron track. The muon p_T is obtained from the curvature of the corresponding track. The energy of charged hadrons is determined from a combination of their momentum measured in the tracker and the matching ECAL and HCAL energy deposits, corrected for zero-suppression effects and for the response function of the calorimeters to hadronic showers. Finally, the energy of neutral hadrons is obtained from the corresponding corrected ECAL and HCAL energies.

The CMS experiment has a two-level trigger system [29]. The level-1 trigger, composed of custom hardware processors, selects events of interest using information from the calorimeters and muon detectors and reduces the readout rate from the 40 MHz bunch-crossing frequency to a maximum of 100 kHz. The software based high-level trigger uses the full event information, including that from the inner tracker, to reduce the event rate to the 1 kHz that is recorded.

A more detailed description of the CMS detector can be found in Ref. [30].

3 Model and signal simulation

Excited leptons can be produced at a pp collider by a CI that is described by an effective four-fermion Lagrangian

$$\mathcal{L}_{\text{CI}} = \frac{g_*^2}{\Lambda^2}\frac{1}{2} j^\mu j_\mu, \tag{1}$$

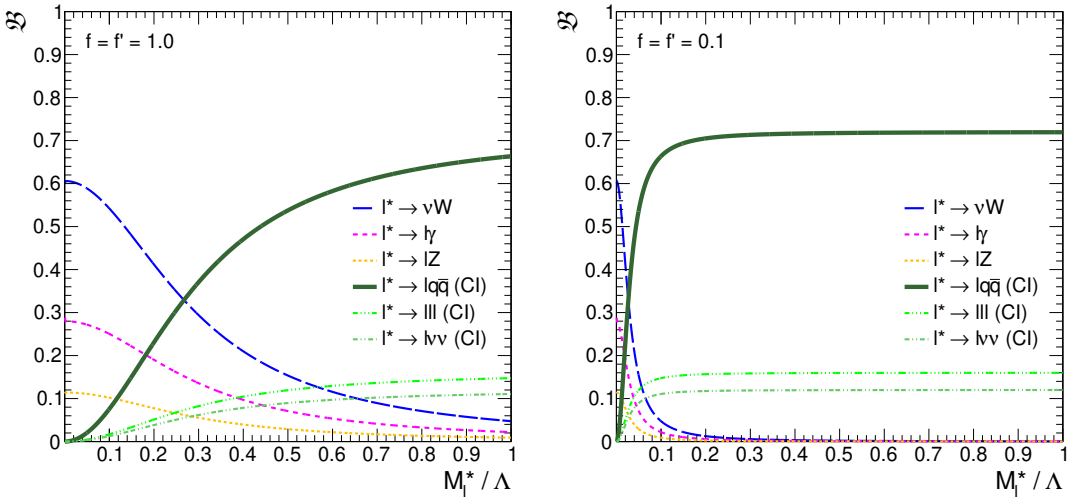

Figure 2: Branching fractions, $\mathcal{B}$, of excited lepton decay channels as a function of the ratio of the excited lepton mass (M_{ℓ^*}) and compositeness scale (Λ) for fixed values of the model parameters $f = f'$, which represent the couplings of excited leptons to SM particles. The branching fraction calculation is based on Ref. [6]. The contact interaction decay to one lepton and two jets, subject of this analysis, is dominating the region of high M_{ℓ^*}/Λ. Couplings f and f' are assumed to be equal to 1 in the left graph, and 0.1 in the right graph.

with the coupling g_*^2 chosen to correspond to 4π, fermion current $j_\mu = \overline{\psi}\gamma_\mu\psi$, and Λ representing the compositeness scale [6]. The excited lepton, ℓ^*, can decay to an SM lepton via a CI $\ell^* \to \ell\psi\overline{\psi}$, where ψ is a fermion, or through the mediation of a gauge boson. The branching fractions of the different decay channels vary as a function of M_{ℓ^*}/Λ, as illustrated in Fig. 2. This analysis complements other searches for excited leptons in the $\ell\ell\gamma$ or $\ell\ell$Z channels and is most sensitive at large values of M_{ℓ^*} and/or Λ. Figure 2 illustrates the rapid increase of the branching fraction of the CI decay to a lepton plus two jets as a function of M_{ℓ^*}/Λ.

The GI transition of excited leptons to SM leptons is described by

$$\mathcal{L}_{\mathrm{GI}} = \frac{1}{2\Lambda}\overline{\psi}_R^\star\sigma^{\mu\nu}\left(gf\frac{\boldsymbol{\tau}}{2}\boldsymbol{W}_{\mu\nu} + g'f'\frac{Y}{2}B_{\mu\nu}\right)\psi_L + \mathrm{h.c.}, \tag{2}$$

where g and g' denote the couplings to the hypercharge and the weak isospin current and f and f' effectively scale the energy scale of the interaction Λ with respect to the CI [6]. Other quantities are $\boldsymbol{W}_{\mu\nu}$ and $B_{\mu\nu}$ denoting the field strength tensors of the SU(2) and U(1) gauge fields with their generators $\boldsymbol{\tau}$ and Y. The partial width of the CI decay is independent of f and f'. Interference between GI and CI transitions is not considered [6]. Since the exact values for f and f' are not known, searches for excited leptons are typically interpreted for two extreme values: $f = f' = 1$ and $f = -f' = 1$. Gauge-interaction decays via photon emission are forbidden for $f = -f'$. However, couplings below unity are also possible and can have a significant impact on the branching fractions, as seen in Fig. 2 (right) for couplings of 0.1. Weaker couplings reduce width for the gauge-interaction decays while enhancing the CI decay. A range of couplings is included in the interpretation of the experimental results.

The production and decay of excited leptons are simulated at leading-order precision with PYTHIA 8.212 [31] using the NNPDF2.3 [32] (in 2016) and NNPDF3.1 [33] (in 2017) parton distribution functions (PDF) and tunes CUETP8M1 (2016) and CP5 (2017) for the underlying event, respectively [34]. Simulated samples are generated for ℓ^* masses of 200, 500, 750 and 1000 GeV and from 1 to 7 TeV in steps of 0.5 TeV. In the simulation, all couplings are set to unity and

Λ to 10 TeV. The specific choice of Λ in the simulation scales the overall cross section for the process, while leaving the kinematic variables unaffected. Hence, the simulated events can be reweighted in order to represent different choices of the couplings and Λ. While the resonance width depends on Λ, it is smaller than the detector resolution for all values used in this analysis. For the example of a 5 TeV signal, the width is of order 15% of the resolution.

At $\Lambda = 10$ TeV and $f = 1$ the product of the cross section and branching fraction for the channel under study ranges from 0.224 fb ($M_{\ell^*} = 200$ GeV), 1.115 fb ($M_{\ell^*} = 1$ TeV), 1.07 $\times 10^{-2}$ fb ($M_{\ell^*} =$ 5 TeV) to 6.91 $\times 10^{-4}$ fb ($M_{\ell^*} = 7$ TeV). For a high-mass ℓ^* signal, each of the decay products will have a p_{T} of approximately 1 TeV, and will tend to be in the central part of the detector.

4 Event reconstruction

The candidate vertex with the largest value of summed physics-object p_{T}^2 is taken to be the primary pp interaction vertex. Here the physics objects are the jets, clustered using the jet finding algorithm [35, 36] with the tracks assigned to the candidate vertices as inputs, and the associated missing transverse momentum, taken as the negative vector p_{T} sum of these jets. In order to suppress background from cosmic ray muons, an event must have at least one primary vertex, with at least five associated well-reconstructed tracks that are within 24 cm in the longitudinal and 2 cm in the transverse direction from the nominal interaction point.

Electrons are reconstructed as ECAL clusters that are matched to a central track and their identification has been optimized for high-p_{T} values [37]. In order to differentiate between electrons and photons, the properties of the track matched to the calorimeter measurement must be consistent with those of an electron originating from the primary vertex. Specifically, there must be $\leq$1 hit missing in the innermost tracker layers, and the transverse distance to the primary vertex must be less than 2 mm (barrel) or less than 5 mm (endcap). Electron candidates are required to have an electron-like shower shape, and to be within the acceptance region of the barrel ($|\eta| < 1.44$) or the endcaps ($1.56 < |\eta| < 2.50$), thus avoiding the transition region between the barrel and the endcap parts of the ECAL. The lateral spread of energy deposited in the ECAL must be consistent with that of a single electron, and the track must be matched to the ECAL cluster must be consistent with a particle originating from the nominal interaction point. The associated energy in the HCAL around the electron direction must be less than 5% of the reconstructed energy of the electron, once noise and pileup are taken into account. To ensure isolation, the scalar sum of the p_{T} of all tracker and calorimeter objects in a cone of radius $\Delta R = \sqrt{(\Delta\phi)^2 + (\Delta\eta)^2} < 0.3$ where ϕ is azimuthal angle in radians, must be less than 3% of the electron p_{T}. Only well-measured tracks that are consistent with originating from the same vertex as the electron are included in the isolation cone.

The muon system covers the pseudorapidity region $|\eta| < 2.4$. The reconstruction of muons is optimized for high-p_{T} values [37]. Measurements from the inner tracker and the outer muon system are combined. The tracker track must have a transverse impact parameter $d_{xy} < 2$ mm with respect to the primary vertex. The longitudinal distance of the tracker track from the primary vertex must be less than 5 mm. Each muon track is required to have at least one hit in the pixel detector, at least six tracker layer hits, and segments with hits in two or more muon detector stations. Since segments are typically in consecutive layers separated by thick layers of steel, the latter requirement significantly reduces the amount of hadronic punch-through [38]. In order to suppress muons with mismeasured p_{T}, an additional requirement $\sigma_{p_{\mathrm{T}}}/p_{\mathrm{T}} < 0.3$ is applied, where $\sigma_{p_{\mathrm{T}}}$ is the p_{T} uncertainty from the muon track reconstruction. Muon isolation requires that the scalar p_{T} sum of all tracks originating from the interaction vertex within a

$\Delta R < 0.3$ cone around its direction, excluding the muon itself, is less than 10% of the muon's p_T.

This analysis uses η- and p_T-dependent scale factors to correct the simulated event yields for the measured differences in the trigger, reconstruction, and identification efficiencies as compared with data.

For each event, hadronic jets are clustered from the reconstructed particle-flow objects with the infrared and collinear safe anti-k_T jet clustering algorithm [35, 36] using a distance parameter of $R = 0.4$. Jet momentum is determined as the vectorial sum of all particle momenta in the jet, and is found from simulation to be, on average, within 5 to 10% of the true momentum over the whole p_T spectrum and detector acceptance. Additional proton-proton interactions within the same or nearby bunch crossings can contribute additional tracks and calorimetric energy depositions, increasing the apparent jet momentum. To mitigate this effect, tracks identified as originating from pileup vertices (contributions from additional pp interactions in the same or nearby bunch crossings) are discarded. Jet energy corrections are derived from simulation studies so that the average measured response of jets becomes identical to that of particle level jets. In situ measurements of the momentum balance in dijet, photon+jet, Z+jet, and multijet events are used to determine any residual differences between the jet energy scale in data and in simulation, and appropriate corrections are made [39]. Additional selection criteria are applied to each jet to remove jets potentially dominated by instrumental effects or reconstruction failures.

5 Backgrounds

Because the final state contains two opposite-sign leptons, the main background originates from Drell–Yan (DY) production. These events are simulated using the NLO generator MADGRAPH5_aMC@NLO v2.2.2 [40, 41] with up to two final-state partons, and are hadronized with PYTHIA 8.212. Because large mass lepton pairs associated with large hadronic activity are a small fraction of all DY events, additional high mass simulations are used to ensure sufficient statistics to evaluate this background. The cross section is normalized to next-to-next-to-leading-order (NNLO) QCD and next-to-leading-order (NLO) EWK using a di-lepton mass-dependent K factor [37, 42].

Another important background is the $t\bar{t}$ process, which yields two prompt leptons if both top quarks decay semi-leptonically. This becomes the dominant background in the medium-mass validation region (VR), as will be described in Section 6. It is simulated with POWHEG 2.0 [43–47] in combination with PYTHIA 8.212 for hadronization. Dedicated high-mass $t\bar{t}$ samples are used to provide sufficient number of events to estimate the background contribution to the high-mass signal region, and are simulated with the same method as used for the main $t\bar{t}$ sample. The cross section is normalized to NNLO [48]. Production of single top quarks in association with a W-boson or in the t-channel production are simulated with POWHEG. The single top s-channel is simulated with MADGRAPH5_aMC@NLO.

Several multi-boson processes can also yield at least two leptons. However, because they have small cross sections, they are sub-dominant backgrounds in this search. The WW, WZ, and ZZ processes with at least two leptons are simulated with POWHEG and MADGRAPH5_aMC@NLO. Triple-boson processes are neglected because of their small cross sections.

The W+jets production can contribute to the signal region when jets are misidentified as electrons. In contrast, the misidentification of muons is negligible. The W+jets production is sim-

ulated to leading order with MADGRAPH5_aMC@NLO v2.2.2 [40, 41]. In addition, high-H_T W samples are also used, where H_T is defined as the sum of jet transverse momenta. The W+jets cross section is normalized to NNLO by application of a K-factor of 1.21 [42].

The background samples are simulated using the NNPDF2.3 or NNPDF3.0 [49] PDF sets with tune CUETP8M1 (in 2016) and the NNPDF3.1 (in 2017) PDF set with CP5 (2017) for the underlying event, respectively [34]. All generated events are processed through a full simulation of the CMS detector based on GEANT4 [50], a trigger emulation, and the event reconstruction chain. All simulated event samples are normalized to the integrated luminosity of the recorded data. The simulation of pileup is included in all events by superimposing simulated minimum bias interactions. For the data set used, the average number of interactions per bunch crossing after selection is about 23 in 2016 and about 30 in 2017, with maximum values of 55 and 70, respectively.

6 Event selection and validation regions

Events with electrons in the final state were selected using a trigger that requires an electromagnetic cluster (electron or photon) with transverse momenta larger than 175 GeV (for 2016) and 200 GeV (for 2017). The efficiency plateaus at 98.5% [51] as a function of pt above a turn-on region and is independent of η, ϕ, p_T, and pileup. Events with muons in the final state were triggered with the single-muon trigger with a minimum p_T of 50 GeV. The muon-trigger efficiency plateaus at an average value of 98% [51] as a function of p_T above the turn-on region and is independent of η, ϕ, and pileup.

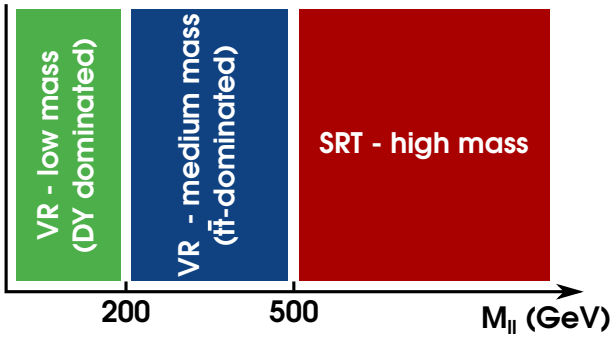

Figure 3: Definition of the two validation regions (VR) and the high-mass signal region (SRT).

Final state particles (electrons, muons and jets) are reconstructed as described in Section 4. The two highest p_T (leading) leptons are selected along with the two leading jets. The p_T thresholds for the leading lepton are 230 GeV (electron) and 53 GeV (muon), chosen to be above the respective trigger turn-on regions. The subleading electrons or muons are required to have an offline p_T of at least 35 and 25 GeV, respectively. Jets are required to have a minimum p_T of 50 GeV. Events with more than the two selected same-flavor leptons are rejected, to reduce background from diboson production.

The majority of the DY background is suppressed by requiring $M_{\ell\ell} > 500$ GeV, constituting the *high-mass signal region (SRT)*. Two VRs are then defined, illustrated in Fig. 3, to verify agreement between data and simulation in different mass regions. The *low-mass VR* with $M_{\ell\ell} < 200$ GeV serves as the VR for DY, which is the dominant background for this final state. The subleading $t\bar{t}$ background tends to populate the *medium-mass VR*, which is defined by 200 GeV $< M_{\ell\ell} <$ 500 GeV. While the low-mass VR is nearly signal free, the medium-mass VR potentially contains a very small fraction of signal events. The signal contamination in the medium VR is far below 1% for the interesting mass range of M_{ℓ^*} above 3.8 TeV.

The invariant mass of the combination of both selected leptons and the two leading jets, $M_{\ell\ell jj}$, is used as the discriminating variable as it provides the best separation power between signal and background. The distributions of other possible variables were studied, but their use yielded lower signal significance. The event distributions as functions of the four-body mass for the low-mass and medium-mass validation regions are shown in Figs. 4 and 5, respectively. The good agreement between experimental and simulated data justifies estimating the background expectation from simulation.

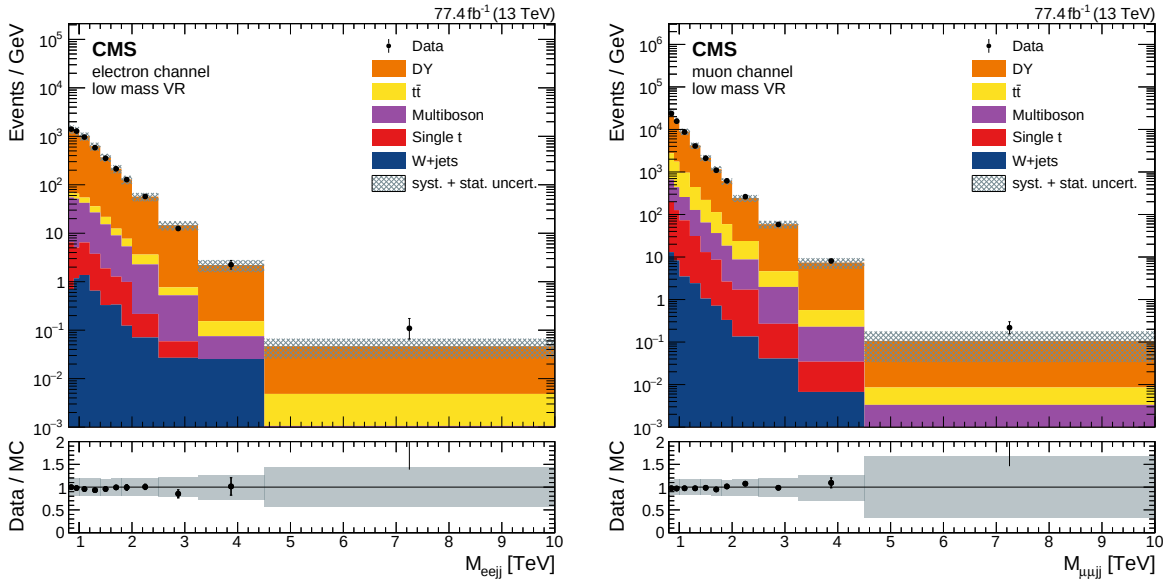

Figure 4: Event distributions as a function of the four-body invariant $M_{\ell\ell jj}$ mass for the electron (left) and muon (right) channels, for the low-mass validation region defined by $M_{\ell\ell} < 200\,\text{GeV}$. The bin content is normalized to the width of the first bin, i.e., 100 GeV. The lower panels show the ratio of data to the simulated SM background, with the shaded band representing the uncertainty.

The signal efficiency, defined as the product of acceptance and detection efficiency of the fraction of reconstructed $2\ell 2\text{j}$ events, resulting from these event selections is shown as a function of the simulated excited lepton mass in Fig. 6. The uncertainties in the figure are only statistical uncertainties. The systematic uncertainties on the product of acceptance and efficiency are between 6 and 8%. The efficiency reaches a plateau of about 55% for the electron channel and 73% for the muon channel. For lower masses, in particular for $M_{\ell^*} < 1\,\text{TeV}$, the acceptance is reduced by the offline p_T thresholds on the objects but this mass region is not of primary interest given previous exclusion limits. For masses above 6 TeV, the efficiency starts to drop slightly because of a growing fraction of events produced off-shell. At the given center-of-mass energy of the LHC, the available energy for generating such heavy particles is limited.

7 Systematic uncertainties

Systematic uncertainties in this analysis can affect the overall normalization and also the shape of the distributions. Uncertainties in the energy scale of different physics objects are taken into account by analyzing the shape of the four-body mass distributions, with the energy scale shifted up and down by $1\,\sigma$. The electron energy scale uncertainty is estimated to be 0.2% in the barrel and 0.3% in the endcap [52]. For muons, the momentum scale is determined using the generalized endpoint method [27] and applied as a function of the η and ϕ of the muon. The

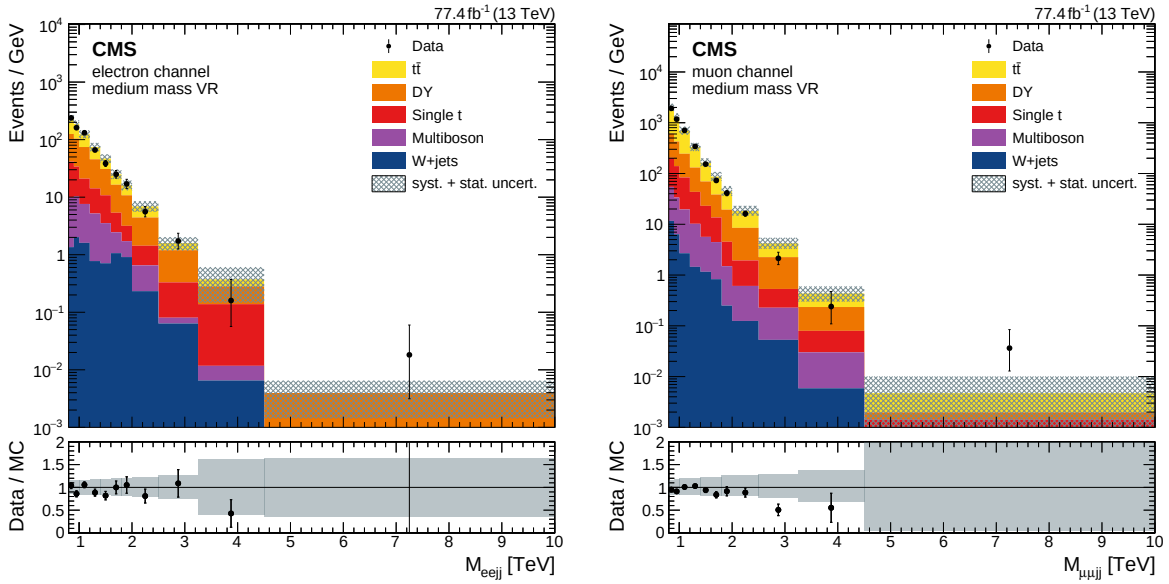

Figure 5: Event distribution as a function of the four-body invariant mass $M_{\ell\ell jj}$ for the electron (left) and muon (right) channels, for the medium-mass validation region defined by $200 < M_{\ell\ell} < 500$ GeV. The bin content is normalized to the width of the first bin, i.e., 100 GeV. The lower panel shows the ratio of data to the simulated SM background, with the shaded band representing the uncertainty.

studies indicate the absence of a significant curvature bias, within an uncertainty of 0.02/TeV in the central region and up to 0.1/TeV in the more forward regions. For jets, the uncertainties associated with the jet energy correction are used [39].

The simulated energy resolution is better than that measured in data. To account for this, jet energy resolution corrections are applied to jets and their uncertainties are considered as a systematic effect [39]. For electrons, the momentum is smeared by 1.2 and 2.4% for barrel and endcaps, respectively [52]. For muons, the momentum is smeared by 5% [27]. These three uncertainties change the shape of the background.

There are systematic uncertainties on the scale factors applied to correct for the differences in the triggering, reconstruction and identification efficiencies between simulation and data. These uncertainties are typically a few percent and are taken into account as normalization uncertainty [27, 52]. The integrated luminosity of the data collected has an uncertainty of 2.5 [53] and 2.3% [54] for the 2016 and 2017 data sets, respectively. The uncertainty due to the modeling of pileup is found to be less than 10% and is by derived by varying the total inelastic pp cross section by 5% [55]. It is treated as an uncertainty in the background shape.

The uncertainty associated with the choice of PDFs affects the cross section of the simulated samples and is taken into account by following an approach outlined by the PDF4LHC recipe [56]. The PDF set used to calculate the variations is NNPDF3.0, for background and signal samples in 2016, and NNPDF3.1, in 2017. Overall, the variation is found to range from 5% at 1 TeV to 60% at 6 TeV, as taken from LHAPDF6.2 [57].

The renormalization and factorization scales provide a handle to estimate the uncertainty due to missing higher orders. Both scales are varied simultaneously by a factor 2 up and down, resulting in different event-by-event weights and an uncertainty of 10 to 30% between 1 and 6 TeV.

In the signal region, the limited number of simulated background events results in a statistical

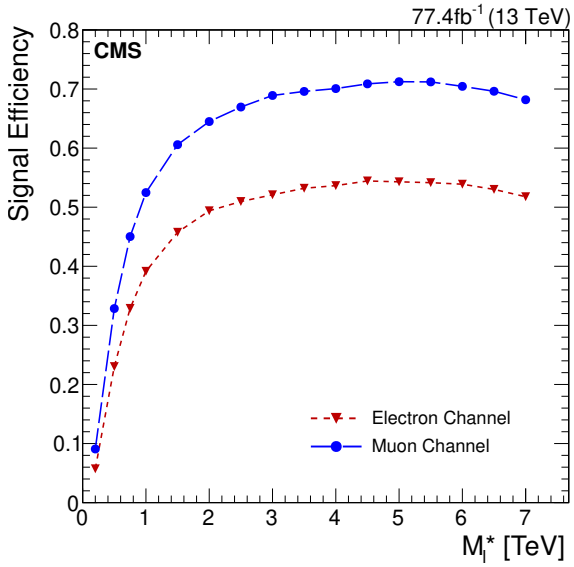

Figure 6: Signal efficiency after all selections are applied, as a function of the excited lepton mass M_{ℓ^*}, based on simulated events.

uncertainty of up to 40% in the background prediction.

Production of W+jets production can contribute to the background when a jet is misidentified as a lepton, albeit at a very small level. A conservative systematic uncertainty of 100% is applied to the W+jets background contribution and reflects the uncertainty in the lepton misidentification rate in the simulation as compared with data.

For the SM background, the dominant sources of uncertainties are the Monte–Carlo (MC) sample sizes and the PDF uncertainty.

8 Results

Event distributions for the signal regions as a function of the four-body invariant mass are shown for the electron and muon channels in Fig. 7. The final distribution is dominated by $\mathrm{t\bar{t}}$ background in the low-mass region and DY background in the high mass region despite being strongly suppressed by the dilepton invariant mass cut. The expected background in the highest mass bin, of more than 5 TeV width, is far less than one event. The analysis would not benefit from reducing the background further at the cost of signal efficiency. The event yields in data compared to the total expected SM backgrounds are given in Table 1 for a number of bins of the discriminating four-body $2\ell 2j$ mass distribution. Also shown are the expectations for potential ℓ^* signals with two different sets of model parameter values: a mass M_{ℓ^*} of 2 TeV and compositeness scale Λ of 10 TeV; and $M_{\ell^*} = \Lambda = 5$ TeV, which roughly corresponds to the maximum sensitivity of this analysis.

No indication of a signal is observed. The limits on the excited lepton mass, M_{ℓ^*}, are calculated using the Bayesian method [58] with a uniform positive prior probability distribution for the signal cross section. Systematic uncertainties in the expected signal and background yields are included either via nuisance parameters with log-normal prior distributions or with the shape of the distribution included through the use of a binned likelihood.

Limits at 95% confidence level (CL) on the product of cross section and branching fraction assuming the proper branching fraction for $M_{\ell^*} = \Lambda$ and $f = f' = 1$ are shown in Fig. 8, and

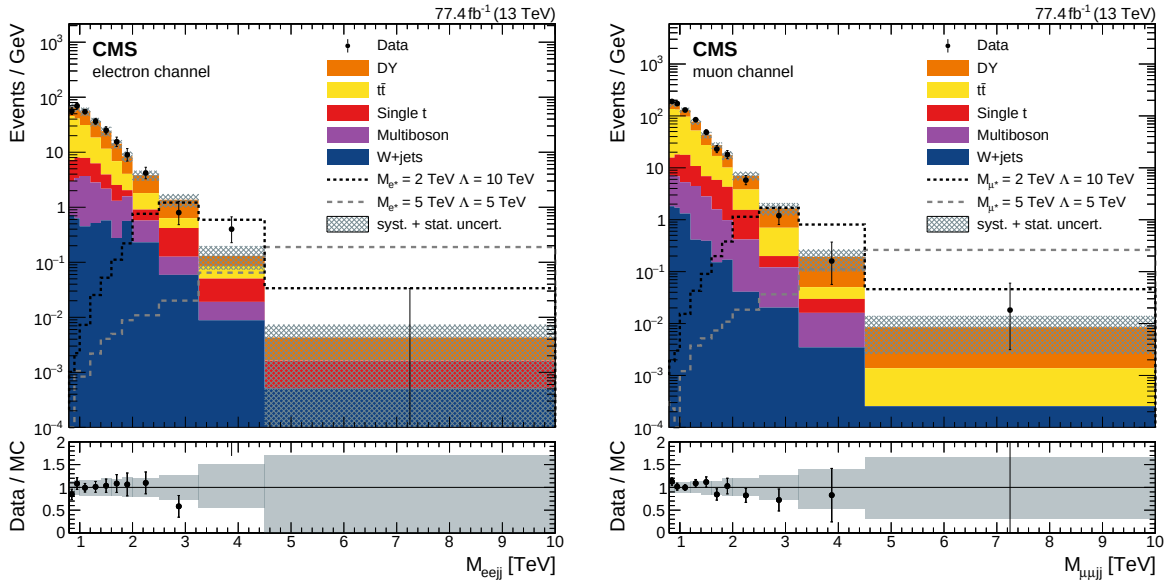

Figure 7: Distribution of the two-lepton two-jet invariant mass in the signal region ($M_{\ell\ell} > 500\,\text{GeV}$) for the electron (left) and muon (right) channels. The example signal shape for two excited lepton masses is indicated as a gray line with the parameters given in the legend and for the benchmark case where the couplings f and f' are set to unity. The bin content is normalized to the width of the first bin, i.e., 100 GeV. The lower panels show the ratio of data to simulation with the total uncertainty in gray.

range from 10 to 0.1 fb, depending on the mass of the excited lepton.

This analysis excludes excited electrons and excited muons at 95% CL for values of M_{ℓ^*} below 5.6 and 5.7 TeV, respectively, assuming that Λ is equal to the mass of the excited leptons. These are the best limits to date on excited electrons and muons. At low masses, the sensitivity is determined by the acceptance and analysis selection. At very high mass, the sensitivity becomes limited by the cross section. The sensitivity to the maximum ℓ^* mass is not affected by the coupling strength.

The cross section limit can be re-evaluated in terms of the compositeness scale Λ as a function of the excited lepton mass. This sensitivity does depend on the coupling strength. Figures 9–11 show the variations in the compositeness scale Λ for the gauge couplings $|f|$ and $|f'|$ equal to unity, for $|f|$ and $|f'|$ equal to 0.1, and for f and f' equal to zero, respectively. Compositeness scales below 5 TeV are excluded for all investigated ℓ^* masses. Maximum sensitivity to Λ is reached at low masses, as is typical for excited lepton searches. The exact mass for this peak sensitivity depends on the coupling scenario, decreasing with weaker GI couplings, and can easily be understood from Fig. 2. Detailed numbers are given in Table 2. In the case of $f = f' = 1$, compositeness scales up to 11 TeV (e*) and 12 TeV (μ^*) are excluded, with the maximum sensitivity for ℓ^* masses around 2 TeV. With values for $f = f' = 0.1$, the decay width to a CI increases, yielding a higher Λ sensitivity of 17 TeV (e*) and 19 TeV (μ^*), respectively, for ℓ^* masses around 1.5 TeV. Assuming zero GI couplings, the observed Λ sensitivity increases to 18 TeV (e*) and 22 TeV (μ^*), respectively, for ℓ^* masses around 1 TeV. While the expected sensitivities in the electron and muon channels are comparable, the observed muon channel sensitivity is up to one standard deviation higher due to fluctuations in the data. For M_{ℓ^*} above 2 TeV these are the best limits to date. In the scenario $f = -f'$, where $\ell\ell\gamma$ has no sensitivity, this CI channel provides the best test of high compositeness scales.

Table 1: Observed event yields in bins of four-body mass compared to the expected SM background, for the $2e2j$ and $2\mu 2j$ final states. Also shown are the expected event yields for two simulated signal samples with the given masses and couplings. All yields are given in bins of the discriminating four-body mass ($2\ell 2j$) distribution, with lower and upper value for each bin given in units of GeV. Systematic uncertainties, as described in the text, are shown.

	Bins in $2\ell 2j$ mass (GeV)				
	500–1500	1500–2500	2500–3500	3500–4500	4500–10000
Data in $2e2j$	368	91	6	5	0
SM prediction	390^{+60}_{-65}	85 ± 16	10.8 ± 3.0	1.1 ± 0.5	$0.24^{+0.17}_{-0.24}$
$f = f' = 1$					
$M_{e^*} = 2\,\text{TeV}, \Lambda = 10\,\text{TeV}$	0.11 ± 0.01	4.5 ± 0.3	11.4 ± 0.7	5.1 ± 0.4	1.9 ± 0.2
$M_{e^*} = 5\,\text{TeV}, \Lambda = 5\,\text{TeV}$	0.011 ± 0.002	0.09 ± 0.01	0.24 ± 0.02	$0.72^{+0.07}_{-0.06}$	10.4 ± 0.7
$f = f' = 0.1$					
$M_{e^*} = 2\,\text{TeV}, \Lambda = 10\,\text{TeV}$	0.34 ± 0.03	13.7 ± 0.9	34.8 ± 2.1	15.6 ± 1.2	5.8 ± 0.6
$M_{e^*} = 5\,\text{TeV}, \Lambda = 5\,\text{TeV}$	0.012 ± 0.002	0.09 ± 0.01	0.25 ± 0.02	$0.76^{+0.07}_{-0.06}$	10.9 ± 0.7
Data in $2\mu 2j$	949	151	11	0	1
SM prediction	949^{+100}_{-115}	161^{+23}_{-25}	13.7 ± 3.7	1.2 ± 0.6	$0.48^{+0.31}_{-0.32}$
$f = f' = 1$					
$M_{\mu^*} = 2\,\text{TeV}, \Lambda = 10\,\text{TeV}$	0.19 ± 0.01	$7.0^{+0.3}_{-0.2}$	$15.8^{+0.7}_{-0.4}$	$7.0^{+0.4}_{-0.3}$	2.5 ± 0.2
$M_{\mu^*} = 5\,\text{TeV}, \Lambda = 5\,\text{TeV}$	0.015 ± 0.002	0.14 ± 0.01	$0.42^{+0.03}_{-0.02}$	1.2 ± 0.1	$14.4^{+1.2}_{-0.4}$
$f = f' = 0.1$					
$M_{\mu^*} = 2\,\text{TeV}, \Lambda = 10\,\text{TeV}$	0.58 ± 0.03	$21.4^{+0.9}_{-0.6}$	$48.2^{+2.1}_{-1.2}$	$21.4^{+1.2}_{-0.9}$	7.6 ± 0.6
$M_{\mu^*} = 5\,\text{TeV}, \Lambda = 5\,\text{TeV}$	0.016 ± 0.002	0.15 ± 0.01	$0.44^{+0.03}_{-0.02}$	1.3 ± 0.1	$15.1^{+1.3}_{-0.4}$

9 Summary

A search for excited leptons decaying via a contact interaction to final states of two electrons or two muons and two resolved jets has been performed. This channel complements other searches for excited leptons. It has greatest sensitivity at large values of the excited lepton mass M_{ℓ^*}. The data for this analysis were recorded with the CMS detector in the years 2016 and 2017, corresponding to a total integrated luminosity of 77.4 fb^{-1} of proton-proton collisions at a center-of-mass energy of 13 TeV.

No significant deviations from SM expectations are observed in the signal region and 95% exclusion limits have been set. Excited electrons (muons) up to masses of $M_{e^*} = 5.6\,\text{TeV}$ ($M_{\mu^*} = 5.7\,\text{TeV}$) are excluded with the usual assumption of $M_{\ell^*} = \Lambda$. These are the best limits to date. The limit was also re-evaluated in terms of the substructure scale Λ, leading to limits of $\Lambda = 11$ and 12 TeV for excited electrons and muons, respectively, for mass values around 2 TeV and couplings of unity. When studying weaker gauge couplings, the limit on the maximum M_{ℓ^*} does not change, but the larger cross section increases the Λ sensitivity at lower masses. For couplings around zero, where the $\ell\ell\gamma$ decay has no sensitivity, limits around 20 TeV for the compositeness scale Λ are achieved.

Acknowledgments

We congratulate our colleagues in the CERN accelerator departments for the excellent performance of the LHC and thank the technical and administrative staffs at CERN and at other CMS

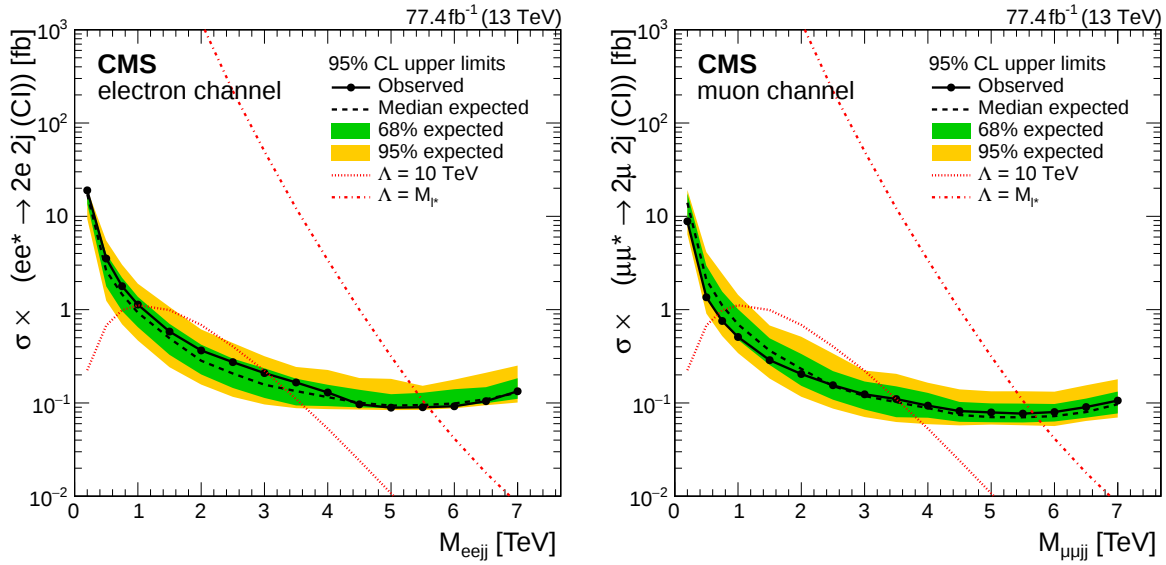

Figure 8: Limits at 95% CL on the product of the production cross section and branching fraction for $\ell\ell^* \to \ell\ell jj$, as a function of the invariant mass $M_{\ell\ell jj}$, for the electron (left) and muon (right) channels. The expectation from the model is represented for $|f| = |f'| = 1$ by two cases, $\Lambda = 10\,\text{TeV}$, and $\Lambda = M_{\ell^*}$.

Table 2: Summary of the observed (expected) limits on ℓ^* mass, assuming $M_{\ell^*} = \Lambda$, for the cases $f = f'$ and $f = -f'$. The limits evaluated in terms of the compositeness scale Λ are shown in the right column.

Search channel	Coupling strength	$M_{\ell^*} = \Lambda$, values in TeV $f = f'$	$f = -f'$	Limit on Λ, in TeV
$\text{ee}^* \to 2\text{e}2j$	$f = 1$	5.6 (5.6)	5.6 (5.6)	11 (11) for $M_{\ell^*} \approx 2\,\text{TeV}$
	$f = 0.1$	5.6 (5.6)	5.6 (5.6)	17 (18) for $M_{\ell^*} \approx 1.5\,\text{TeV}$
	$f = 0$	5.6 (5.6)	5.6 (5.6)	18 (19) for $M_{\ell^*} \approx 1\,\text{TeV}$
$\mu\mu^* \to 2\mu 2j$	$f = 1$	5.7 (5.7)	5.7 (5.7)	12 (12) for $M_{\ell^*} \approx 2\,\text{TeV}$
	$f = 0.1$	5.7 (5.7)	5.7 (5.7)	19 (19) for $M_{\ell^*} \approx 1.5\,\text{TeV}$
	$f = 0$	5.7 (5.7)	5.7 (5.7)	22 (20) for $M_{\ell^*} \approx 1\,\text{TeV}$

institutes for their contributions to the success of the CMS effort. In addition, we gratefully acknowledge the computing centers and personnel of the Worldwide LHC Computing Grid for delivering so effectively the computing infrastructure essential to our analyses. Finally, we acknowledge the enduring support for the construction and operation of the LHC and the CMS detector provided by the following funding agencies: BMBWF and FWF (Austria); FNRS and FWO (Belgium); CNPq, CAPES, FAPERJ, FAPERGS, and FAPESP (Brazil); MES (Bulgaria); CERN; CAS, MoST, and NSFC (China); COLCIENCIAS (Colombia); MSES and CSF (Croatia); RPF (Cyprus); SENESCYT (Ecuador); MoER, ERC IUT, PUT and ERDF (Estonia); Academy of Finland, MEC, and HIP (Finland); CEA and CNRS/IN2P3 (France); BMBF, DFG, and HGF (Germany); GSRT (Greece); NKFIA (Hungary); DAE and DST (India); IPM (Iran); SFI (Ireland); INFN (Italy); MSIP and NRF (Republic of Korea); MES (Latvia); LAS (Lithuania); MOE and UM (Malaysia); BUAP, CINVESTAV, CONACYT, LNS, SEP, and UASLP-FAI (Mexico); MOS (Montenegro); MBIE (New Zealand); PAEC (Pakistan); MSHE and NSC (Poland); FCT (Portugal); JINR (Dubna); MON, RosAtom, RAS, RFBR, and NRC KI (Russia); MESTD (Serbia); SEIDI, CPAN, PCTI, and FEDER (Spain); MOSTR (Sri Lanka); Swiss Funding Agencies (Switzerland); MST (Taipei); ThEPCenter, IPST, STAR, and NSTDA (Thailand); TUBITAK and TAEK (Turkey);

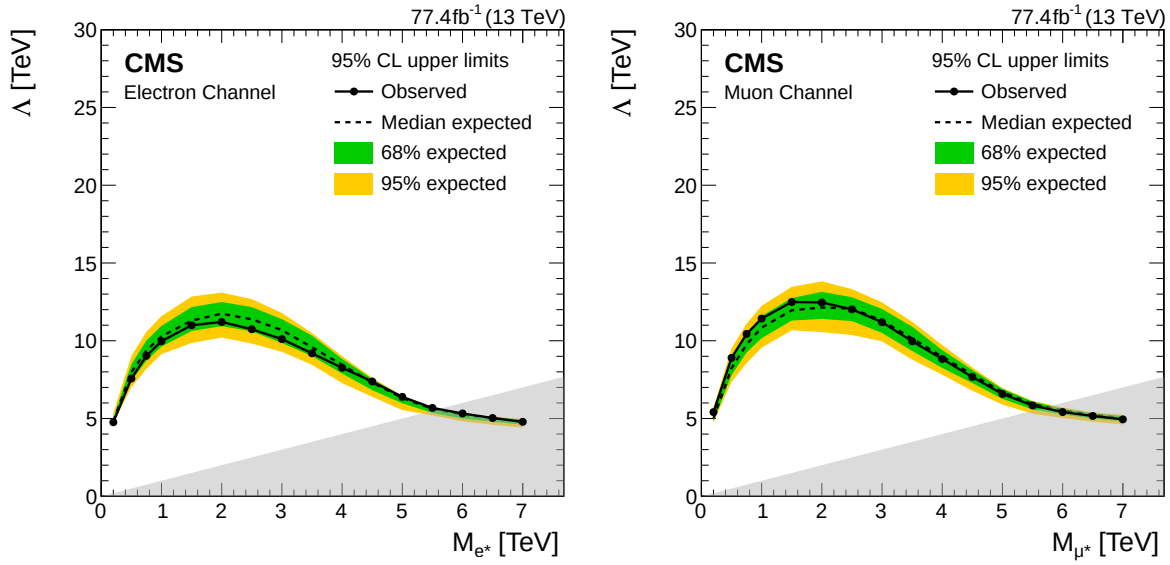

Figure 9: Limits on the compositeness scale Λ for the electron (left) and muon (right) channels, as a function of the mass of the excited lepton, for the benchmark case where the GI couplings $|f|$ and $|f'|$ are set to one. The model is not valid in the hatched area.

NASU (Ukraine); STFC (United Kingdom); DOE and NSF (USA).

Individuals have received support from the Marie-Curie program and the European Research Council and Horizon 2020 Grant, contract Nos. 675440, 752730, and 765710 (European Union); the Leventis Foundation; the A.P. Sloan Foundation; the Alexander von Humboldt Foundation; the Belgian Federal Science Policy Office; the Fonds pour la Formation à la Recherche dans l'Industrie et dans l'Agriculture (FRIA-Belgium); the Agentschap voor Innovatie door Wetenschap en Technologie (IWT-Belgium); the F.R.S.-FNRS and FWO (Belgium) under the "Excellence of Science – EOS" – be.h project n. 30820817; the Beijing Municipal Science & Technology Commission, No. Z191100007219010; the Ministry of Education, Youth and Sports (MEYS) of the Czech Republic; the Deutsche Forschungsgemeinschaft (DFG) under Germanys Excellence Strategy – EXC 2121 "Quantum Universe" – 390833306; the Lendület ("Momentum") Program and the János Bolyai Research Scholarship of the Hungarian Academy of Sciences, the New National Excellence Program ÚNKP, the NKFIA research grants 123842, 123959, 124845, 124850, 125105, 128713, 128786, and 129058 (Hungary); the Council of Science and Industrial Research, India; the HOMING PLUS program of the Foundation for Polish Science, cofinanced from European Union, Regional Development Fund, the Mobility Plus program of the Ministry of Science and Higher Education, the National Science Center (Poland), contracts Harmonia 2014/14/M/ST2/00428, Opus 2014/13/B/ST2/02543, 2014/15/B/ST2/03998, and 2015/19/B/ST2/02861, Sonata-bis 2012/07/E/ST2/01406; the National Priorities Research Program by Qatar National Research Fund; the Ministry of Science and Education, grant no. 14.W03.31.0026 (Russia); the Programa Estatal de Fomento de la Investigación Científica y Técnica de Excelencia María de Maeztu, grant MDM-2015-0509 and the Programa Severo Ochoa del Principado de Asturias; the Thalis and Aristeia programs cofinanced by EU-ESF and the Greek NSRF; the Rachadapisek Sompot Fund for Postdoctoral Fellowship, Chulalongkorn University and the Chulalongkorn Academic into Its 2nd Century Project Advancement Project (Thailand); the Kavli Foundation; the Nvidia Corporation; the SuperMicro Corporation; the Welch Foundation, contract C-1845; and the Weston Havens Foundation (USA).

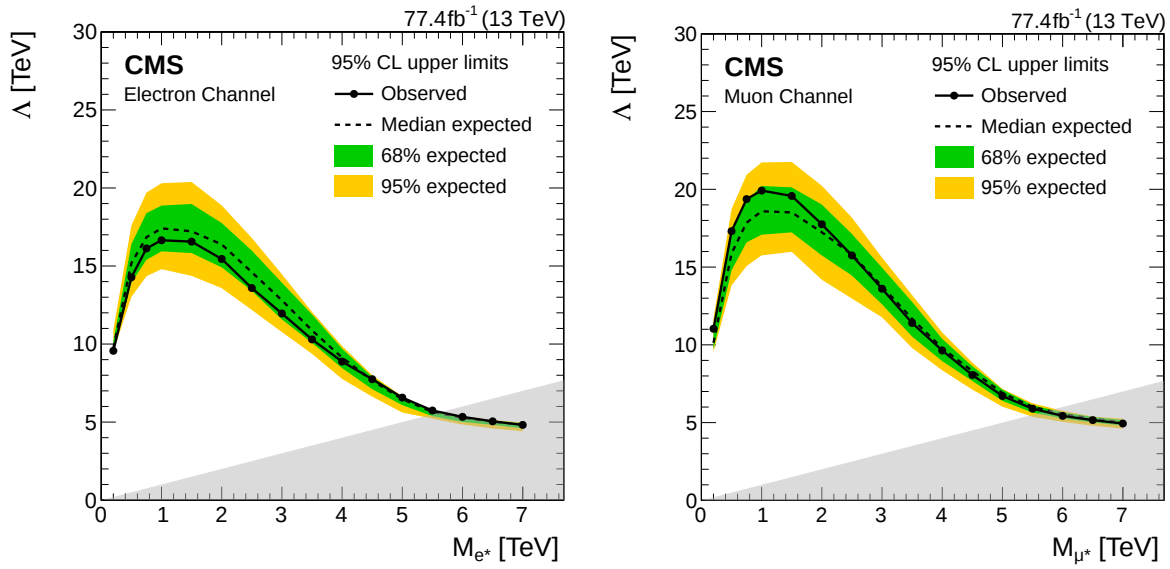

Figure 10: Limits on the compositeness scale Λ for the electron (left) and muon (right) channels, as a function of the mass of the excited lepton, for the case where the GI couplings $|f|$ and $|f'|$ are set to 0.1. The model is not valid in the hatched area.

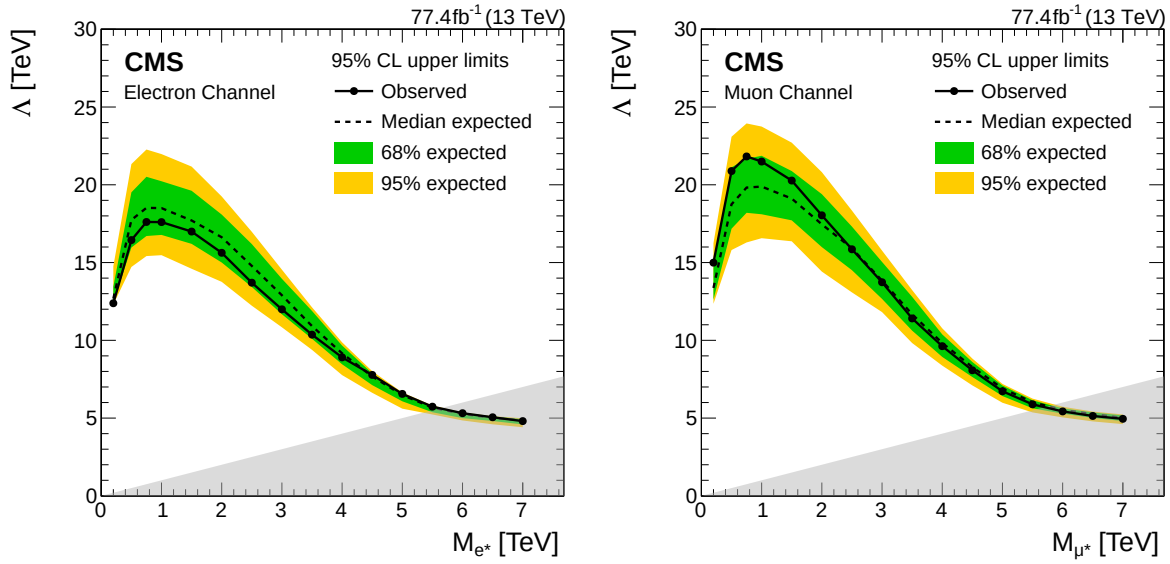

Figure 11: Limits on the compositeness scale Λ for the electron (left) and muon (right) channels, as a function of the mass of the excited lepton, for the benchmark case where the GI couplings f and f' vanish. The model is not valid in the hatched area.

References

[1] J. C. Pati, A. Salam, and J. A. Strathdee, "Are quarks composite?", *Phys. Lett. B* **59** (1975) 265, doi:10.1016/0370-2693(75)90042-8.

[2] H. Terazawa, M. Yasuè, K. Akama, and M. Hayshi, "Observable effects of the possible substructure of leptons and quarks", *Phys. Lett. B* **112** (1982) 387, doi:10.1016/0370-2693(82)91075-9.

[3] E. Eichten, K. D. Lane, and M. E. Peskin, "New tests for quark and lepton substructure", *Phys. Rev. Lett.* **50** (1983) 811, doi:10.1103/PhysRevLett.50.811.

[4] H. Harari, "Composite models for quarks and leptons", *Phys. Rept.* **104** (1984) 159, doi:10.1016/0370-1573(84)90207-2.

[5] K. D. Lane, F. E. Paige, T. Skwarnicki, and W. J. Womersley, "Simulations of supercollider physics", *Phys. Rept.* **278** (1997) 291, doi:10.1016/S0370-1573(96)00018-X, arXiv:hep-ph/9412280.

[6] U. Baur, M. Spira, and P. M. Zerwas, "Excited quark and lepton production at hadron colliders", *Phys. Rev. D* **42** (1990) 815, doi:10.1103/PhysRevD.42.815.

[7] O. W. Greenberg and C. A. Nelson, "Composite models of leptons", *Phys. Rev. D* **10** (1974) 2567, doi:10.1103/PhysRevD.10.2567.

[8] O. W. Greenberg and J. Sucher, "A quantum structure dynamic model of quarks, leptons, weak vector bosons, and Higgs mesons", *Phys. Lett. B* **99** (1981) 339, doi:10.1016/0370-2693(81)90113-1.

[9] S. Biondini, R. Leonardi, O. Panella, and M. Presilla, "Perturbative unitarity bounds for effective composite models", *Phys. Lett. B* **795** (2019) 644, doi:10.1016/j.physletb.2019.134990, arXiv:1903.12285. [Erratum: doi:10.1016/j.physletb.2019.06.042].

[10] ALEPH Collaboration, "Search for excited leptons at 130–140 GeV", *Phys. Lett. B* **385** (1996) 445, doi:10.1016/0370-2693(96)00961-6.

[11] DELPHI Collaboration, "Search for composite and exotic fermions at LEP 2", *Eur. Phys. J. C* **8** (1999) 41, doi:10.1007/s100529901074, arXiv:hep-ex/9811005.

[12] OPAL Collaboration, "Search for unstable heavy and excited leptons at LEP 2", *Eur. Phys. J. C* **14** (2000) 73, doi:10.1007/s100520050734, arXiv:hep-ex/0001056.

[13] L3 Collaboration, "Search for excited leptons at LEP", *Phys. Lett. B* **568** (2003) 23, doi:10.1016/j.physletb.2003.05.004, arXiv:hep-ex/0306016.

[14] H1 Collaboration, "Search for excited electrons in ep collisions at HERA", *Phys. Lett. B* **666** (2008) 131, doi:10.1016/j.physletb.2008.07.014, arXiv:0805.4530.

[15] CDF Collaboration, "Search for excited and exotic electrons in the eγ decay channel in p$\overline{\text{p}}$ collisions at $\sqrt{s}$ = 1.96 TeV", *Phys. Rev. Lett.* **94** (2005) 101802, doi:10.1103/PhysRevLett.94.101802, arXiv:hep-ex/0410013.

[16] CDF Collaboration, "Search for excited and exotic muons in the $\mu\gamma$ decay channel in p$\overline{\text{p}}$ collisions at $\sqrt{s}$ = 1.96 TeV", *Phys. Rev. Lett.* **97** (2006) 191802, doi:10.1103/PhysRevLett.97.191802, arXiv:hep-ex/0606043.

[17] D0 Collaboration, "Search for excited muons in $p\overline{p}$ collisions at $\sqrt{s} = 1.96$ TeV", *Phys. Rev. D* **73** (2006) 111102, doi:10.1103/PhysRevD.73.111102, arXiv:hep-ex/0604040.

[18] D0 Collaboration, "Search for excited electrons in $p\overline{p}$ collisions at $\sqrt{s} = 1.96$ TeV", *Phys. Rev. D* **77** (2008) 091102, doi:10.1103/PhysRevD.77.091102, arXiv:0801.0877.

[19] ATLAS Collaboration, "Search for excited electrons and muons in $\sqrt{s} = 8$ TeV proton-proton collisions with the ATLAS detector", *New J. Phys.* **15** (2013) 093011, doi:10.1088/1367-2630/15/9/093011, arXiv:1308.1364.

[20] ATLAS Collaboration, "A search for an excited muon decaying to a muon and two jets in pp collisions at $\sqrt{s} = 8$ TeV with the ATLAS detector", *New J. Phys.* **18** (2016) 073021, doi:10.1088/1367-2630/18/7/073021, arXiv:1601.05627.

[21] ATLAS Collaboration, "Search for excited electrons singly produced in proton-proton collisions at $\sqrt{s} = 13$ TeV with the ATLAS experiment at the LHC", *Eur. Phys. J. C* **79** (2019) 803, doi:10.1140/epjc/s10052-019-7295-1, arXiv:1906.03204.

[22] CMS Collaboration, "Search for excited leptons in pp collisions at $\sqrt{s} = 7$ TeV", *Phys. Lett. B* **720** (2013) 309, doi:10.1016/j.physletb.2013.02.031, arXiv:1210.2422.

[23] CMS Collaboration, "Search for excited leptons in proton-proton collisions at $\sqrt{s} = 8$ TeV", *JHEP* **03** (2016) 125, doi:10.1007/JHEP03(2016)125, arXiv:1511.01407.

[24] CMS Collaboration, "Search for excited leptons in $\ell\ell\gamma$ final states in proton-proton collisions at $\sqrt{s} = 13$ TeV", *JHEP* **04** (2019) 015, doi:10.1007/JHEP04(2019)015, arXiv:1811.03052.

[25] CMS Collaboration, "Performance of photon reconstruction and identification with the CMS detector in proton-proton collisions at $\sqrt{s}$ = 8 TeV", *JINST* **10** (2015) P08010, doi:10.1088/1748-0221/10/08/P08010, arXiv:1502.02702.

[26] CMS Collaboration, "Search for heavy narrow dilepton resonances in pp collisions at $\sqrt{s} = 7$ TeV and $\sqrt{s} = 8$ TeV", *Phys. Lett. B* **720** (2013) 63, doi:10.1016/j.physletb.2013.02.003, arXiv:1212.6175.

[27] CMS Collaboration, "Performance of the CMS muon detector and muon reconstruction with proton-proton collisions at $\sqrt{s} = 13$ TeV", *JINST* **13** (2018) P06015, doi:10.1088/1748-0221/13/06/P06015, arXiv:1804.04528.

[28] CMS Collaboration, "Particle-flow reconstruction and global event description with the CMS detector", *JINST* **12** (2017) P10003, doi:10.1088/1748-0221/12/10/P10003, arXiv:1706.04965.

[29] CMS Collaboration, "The CMS trigger system", *JINST* **12** (2017) P01020, doi:10.1088/1748-0221/12/01/P01020, arXiv:1609.02366.

[30] CMS Collaboration, "The CMS experiment at the CERN LHC", *JINST* **3** (2008) S08004, doi:10.1088/1748-0221/3/08/S08004.

[31] T. Sjöstrand et al., "An introduction to PYTHIA 8.2", *Comp. Phys. Comm.* **191** (2015) 159, doi:10.1016/j.cpc.2015.01.024, arXiv:1410.3012.

[32] NNPDF Collaboration, "Parton distributions with LHC data", *Nucl. Phys. B* **867** (2013) 244, doi:10.1016/j.nuclphysb.2012.10.003, arXiv:1207.1303.

[33] NNPDF Collaboration, "Parton distributions from high-precision collider data", *Eur. Phys. J. C* **77** (2017) 663, doi:10.1140/epjc/s10052-017-5199-5, arXiv:1706.00428.

[34] CMS Collaboration, "Extraction and validation of a new set of CMS PYTHIA8 tunes from underlying-event measurements", *Eur. Phys. J. C* **80** (2020) 4, doi:10.1140/epjc/s10052-019-7499-4, arXiv:1903.12179.

[35] M. Cacciari, G. P. Salam, and G. Soyez, "The anti-k_T jet clustering algorithm", *JHEP* **04** (2008) 063, doi:10.1088/1126-6708/2008/04/063, arXiv:0802.1189.

[36] M. Cacciari, G. P. Salam, and G. Soyez, "FastJet user manual", *Eur. Phys. J. C* **72** (2012) 1896, doi:10.1140/epjc/s10052-012-1896-2, arXiv:1111.6097.

[37] CMS Collaboration, "Search for high-mass resonances in dilepton final states in proton-proton collisions at $\sqrt{s} = 13$ TeV", *JHEP* **06** (2018) 120, doi:10.1007/JHEP06(2018)120, arXiv:1803.06292.

[38] CMS Collaboration, "Performance of CMS muon reconstruction in pp collision events at $\sqrt{s} = 7$ TeV", *JINST* **7** (2012) P10002, doi:10.1088/1748-0221/7/10/P10002, arXiv:1206.4071.

[39] CMS Collaboration, "Jet energy scale and resolution in the CMS experiment in pp collisions at 8 TeV", *JINST* **12** (2017) P02014, doi:10.1088/1748-0221/12/02/P02014, arXiv:1607.03663.

[40] J. Alwall et al., "The automated computation of tree-level and next-to-leading order differential cross sections, and their matching to parton shower simulations", *JHEP* **07** (2014) 079, doi:10.1007/JHEP07(2014)079, arXiv:1405.0301.

[41] R. Frederix and S. Frixione, "Merging meets matching in MADGRAPH5_aMC@NLO", *JHEP* **12** (2012) 061, doi:10.1007/JHEP12(2012)061, arXiv:1209.6215.

[42] R. Gavin, Y. Li, F. Petriello, and S. Quackenbush, "FEWZ 2.0: A code for hadronic Z production at next-to-next-to-leading order", *Comput. Phys. Commun.* **182** (2011) 2388, doi:10.1016/j.cpc.2011.06.008, arXiv:1011.3540.

[43] P. Nason, "A new method for combining NLO QCD with shower Monte Carlo algorithms", *JHEP* **11** (2004) 040, doi:10.1088/1126-6708/2004/11/040, arXiv:hep-ph/0409146.

[44] S. Frixione, P. Nason, and C. Oleari, "Matching NLO QCD computations with parton shower simulations: the POWHEG method", *JHEP* **11** (2007) 070, doi:10.1088/1126-6708/2007/11/070, arXiv:0709.2092.

[45] S. Alioli, P. Nason, C. Oleari, and E. Re, "A general framework for implementing NLO calculations in shower Monte Carlo programs: the POWHEG BOX", *JHEP* **06** (2010) 043, doi:10.1007/JHEP06(2010)043, arXiv:1002.2581.

[46] E. Re, "Single-top W*t*-channel production matched with parton showers using the POWHEG method", *Eur. Phys. J. C* **71** (2011) 1547, doi:10.1140/epjc/s10052-011-1547-z, arXiv:1009.2450.

[47] S. Frixione, P. Nason, and G. Ridolfi, "A positive-weight next-to-leading-order Monte Carlo for heavy flavour hadroproduction", *JHEP* **09** (2007) 126, doi:10.1088/1126-6708/2007/09/126, arXiv:0707.3088.

[48] M. Czakon, P. Fiedler, and A. Mitov, "Total top-quark pair-production cross section at hadron colliders through $\mathcal{O}(\alpha_S^4)$", *Phys. Rev. Lett.* **110** (2013) 252004, doi:10.1103/PhysRevLett.110.252004.

[49] NNPDF Collaboration, "Parton distributions for the LHC Run II", *JHEP* **04** (2015) 040, doi:10.1007/JHEP04(2015)040, arXiv:1410.8849.

[50] S. Agostinelli et al., "GEANT4—a simulation toolkit", *Nucl. Instrum. Meth. A* **506** (2003) 250, doi:10.1016/S0168-9002(03)01368-8.

[51] CMS Collaboration, "Search for high-mass resonances in final states with a lepton and missing transverse momentum at $\sqrt{s} = 13$ TeV", *JHEP* **06** (2018) 128, doi:10.1007/JHEP06(2018)128, arXiv:1803.11133.

[52] CMS Collaboration, "Performance of electron reconstruction and selection with the CMS detector in proton-proton collisions at $\sqrt{s} = 8$ TeV", *JINST* **10** (2015) P06005, doi:10.1088/1748-0221/10/06/P06005, arXiv:1502.02701.

[53] CMS Collaboration, "CMS Luminosity Measurements for the 2016 Data Taking Period", CMS Physics Analysis Summary, CMS-PAS-LUM-17-001, CERN, Geneva, 2017.

[54] CMS Collaboration, "CMS Luminosity Measurements for the 2017 Data Taking Period at $\sqrt{s} = 13$ TeV", CMS Physics Analysis Summary, CMS-PAS-LUM-17-004, CERN, Geneva, 2017.

[55] CMS Collaboration, "Measurement of the inelastic proton-proton cross section at $\sqrt{s} = 13$ TeV", *JHEP* **07** (2018) 161, doi:10.1007/JHEP07(2018)161, arXiv:1802.02613.

[56] J. Butterworth et al., "PDF4LHC recommendations for LHC Run II", *J. Phys. G* **43** (2016) 023001, doi:10.1088/0954-3899/43/2/023001, arXiv:1510.03865.

[57] A. Buckley et al., "LHAPDF6: parton density access in the LHC precision era", *Eur. Phys. J. C* **75** (2015) 132, doi:10.1140/epjc/s10052-015-3318-8, arXiv:1412.7420.

[58] Particle Data Group, M. Tanabashi et al., "Review of particle physics", *Phys. Rev. D* **98** (2018) 030001, doi:10.1103/PhysRevD.98.030001.